A Comparison of Shell and Solid Finite Element Models of Austenitic Stainless Steel Columns in Compression

Daniel Jindra, Zdeněk Kala, Jiří Kala

Brno University of Technology, Faculty of Civil Engineering, Institute of Structural Mechanics, Veveří 331/95, 602 00 Brno, Czech Republic.

jindra.d@fce.vutbr.cz

Abstract. The subject of this article is the implementation of new knowledge on material and geometric characteristics obtained from an experimental research program in advanced numerical modelling of compressed columns made of austenitic stainless steel using the ANSYS Classic software. Nonlinear stress–strain curves were obtained using our own experimental program and studied in terms of identifying the most suitable nonlinear material model. Additional material and geometric characteristics were obtained from literature and other independent research. Numerical models differing in mesh density localization, formulation of element integration, non-linear material model, and initial geometric imperfections were created and compared. The aim of the models was the ultimate limit state of a strut of circular hollow cross-section stressed by compression and analysed using the geometrically and materially nonlinear solution with consideration to the influence of initial imperfections. Static resistance and limit state deformations are compared for each model. The paper presents the analysis of model uncertainty by comparing SHELL and SOLID FE models, which must be characterized before the start of the analysis of the random influence of imperfections on the limit states. The mean values and the coefficients of variation are practically the same for both approaches. In summary, the presented models can be considered sufficiently validated and eligible for integration in tandem with simulation sampling methods.

1. Introduction

Computational modelling is a traditional practice in many technical fields. With the development of computers in recent decades, computational modelling has been integrated into most technical sciences and has become an integral part of the design of structures and bridges [1], structural mechanics [2], engineering geology [3], or operations research [4]. Slender members of steel structures can be modelled using the finite element method utilizing many types of finite elements such as BEAM elements [5, 6], SHELL elements [7, 8], or SOLID elements [9, 10]. Although the conciseness and accuracy of models grow more or less naturally towards SOLID elements, there is also a growing risk of creating a less accurate or an inaccurate model, and many model parameters and other tasks must be set up and addressed to make the model a valuable and useful tool.

The presented article aims to compare computational models created using the SHELL and SOLID finite element method with the inclusion of material and geometric nonlinearities [11]. The paper presents the analysis of the buckling resistance of stainless steel using advanced modelling with consideration to the influence of initial imperfections and material nonlinearities.

2. Experimental Testing Program

Two sets of CHS column specimens, 106×3 (set of 9 different columns), and 104×2 (set of 8 different columns), were tested.

An elaborate description of the experimental program is presented in the study of Mr. Buchanan et al. [12] (p. 298 - 303).

3. Numerical Finite Element Models

Ansys parametric design language (APDL) macros in the environment of ANSYS Classic [13] were used to create the parametric numerical finite element model. Geometrical parameters, amplitudes of initial global imperfection ($\omega_0 + e_0$) (Table 1 – Table 2), and material parameters (Table 3) were considered as the input variables.

3.1. Modelling approaches, Adopted Finite Element formulations

This study compares two varying approaches to numerical modelling. In approach #A, the model is comprised of shell elements, while the model in approach #B is comprised of solid elements.

3.1.1. Modelling Approach #A (shell model). The CHS columns were modelled using SHELL 181 elements (4-node structural shell elements) with 3 translational degrees of freedom (DOF) and 3 rotational DOF per node. Bending and membrane stiffness is present in the elements (Mindlin-Reissner theory), which include the linear effect of transverse shear deformation. The shell elements are rectangular with a maximum edge size of 8 mm in the longitudinal direction and 5 mm in the tangential direction (along the circumference) (Figure 1 a). Reduced integration with hourglass control was used for the modelling with 1 integration point (3 through the thickness). Shear locking was relieved using the shear strain formulation of Bathe-Dvorkin [13].

3.1.2. Modelling Approach #B (solid model). The CHS columns were modelled using the solid structural finite element SOLID 185 (Figure 1 b). The mesh sizes are the same as in approach #A. Three elements were considered in the radial direction, along the cross-section thickness *t*. The selective reduced integration method also known as the B-bar method [13], which prevents volumetric locking in nearly incompressible cases, was considered by selecting the default key option (0) of the element technology.

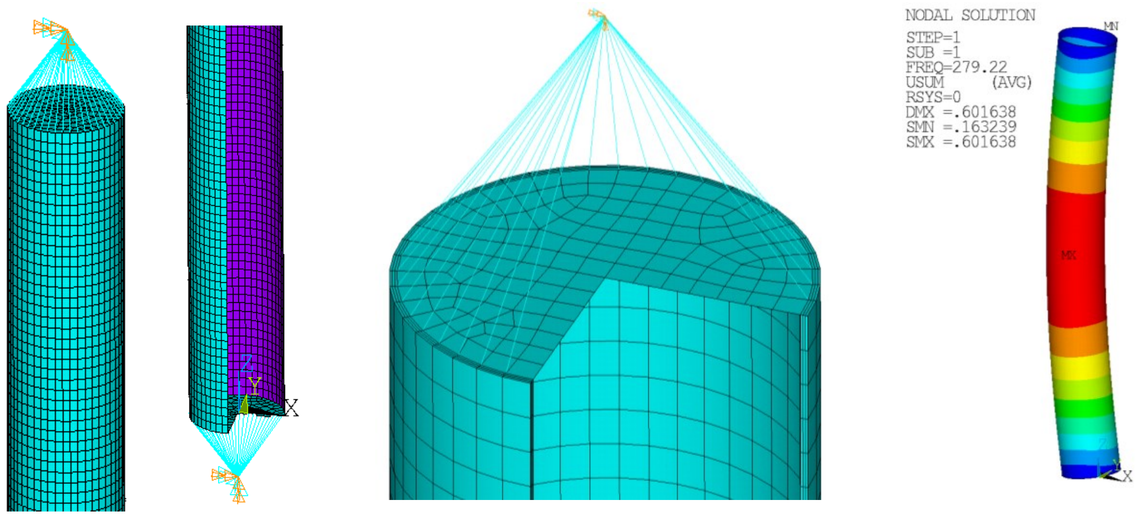

(a) (b) (c)

Figure 1. 104×2-950 specimen: (a) approach #A - shell model geometry; (b) approach #B - solid model geometry; (c) Results of Nodal solution, total displacements

3.2. Geometry of the Numerical Models

The geometric parameters, D (outer diameter of the cross-section), t (wall thickness), L (effective structural length, with consideration to the additional knife edge lengths), and imperfection amplitudes ($\omega_0 + e_0$) were considered according to the measured values of the respective specimens (see Table 1 – Table 2 below, based on data from Table 5 – Table 6 in [12], respectively).

Table 1. Measured geometric parameters of the 106×3 CHS cross-section of the pin-ended columns

Specimen	D [mm]	t [mm]	L [mm]	$L/(\omega_0 + e_0)$ [-]	$(\omega_0 + e_0)$ [mm]
106×3-550-P	105.74	2.78	554.27	1218	0.455
106×3-750-P	105.81	2.88	754.21	1034	0.729
106×3-750-PR	105.77	2.72	754.21	880	0.857
106×3-950-P	105.78	2.79	954.00	957	0.997
106×3-1150-P	105.84	2.83	1154.00	1000	1.154
106×3-1650-P	105.63	2.74	1657.00	945	1.753
106×3-2150-P	105.88	2.71	2152.90	997	2.159
106×3-2650-P	105.64	2.73	2652.50	987	2.687
106×3-3080-P	105.67	2.70	3083.00	1044	2.953

Table 2. Measured geometric parameters of the 104×2 CHS cross-section of the pin-ended columns

Specimen	D [mm]	t [mm]	L [mm]	$L/(\omega_0 + e_0)$ [-]	$(\omega_0 + e_0)$ [mm]
104×2-550-P	103.97	1.89	553.77	1180	0.469
104×2-750-P	104.01	1.89	753.84	887	0.850
104×2-950-P	103.97	1.88	954.00	827	1.154
104×2-1150-P	104.14	1.86	1153.50	1115	1.035
104×2-1650-P	104.09	1.85	1656.60	963	1.720
104×2-2150-P	104.08	1.79	2153.60	999	2.156
104×2-2650-P	103.92	1.75	2653.50	1064	2.494
104×2-3080-P	104.10	1.79	3084.00	1036	2.977

3.3. Geometric Imperfections

Global imperfections were introduced into the FE model using the lowest global buckling modal shape obtained from the prior modal analysis, e.g., see Figure 1 c. Initial global imperfections and eccentricity were simulated using the global imperfection amplitude. The amplitudes of $\omega_0 + e_0$ were considered according to Tables 1 - 2. Local imperfections were neglected, because of relatively small influence on the global results for the considered geometries [11]. Increasing number of scaled buckling modes might be added to the perfect geometry of certain structures to achieve accuracy including the appropriate scaling factors [14]. Such approach was appropriate in order to define the imperfections of more complex structures (frames) [14], however for a single column does not seem to be applicable.

3.4. Material model

The stress-strain relation offered by Ramberg and Osgood [15] and modified by Hill [16] was adopted to describe the behaviour of the stainless steel material:

$$\varepsilon = \frac{\sigma}{E_0} + 0.002 \cdot \left(\frac{\sigma}{\sigma_{0.2}} \right)^n , \tag{1}$$

where σ and ε represent the engineering stress and strain respectively, E_0 is Young's modulus, $\sigma_{0.2}$ is the material 0.2% proof stress, and n is a strain hardening exponent. The model overestimates the stress values at strain values greater than the $\sigma_{0.2}$ value [17]. Closer agreement with experimental data is offered by the 2-stage compound stress-strain curve proposed by Mirambell and Real [18] for stress values higher than the 0.2% proof stress [17]. A modification of the second stage was proposed by Gardner [19] for compressive loading:

$$\varepsilon = \frac{\sigma - \sigma_{0.2}}{E_{0.2}} + \left(0.008 - \frac{\sigma_{1.0} - \sigma_{0.2}}{E_{0.2}}\right) \cdot \left(\frac{\sigma - \sigma_{0.2}}{\sigma_{1.0} - \sigma_{0.2}}\right)^{n'_{0.2,1.0}} + \varepsilon_{t0.2} \Leftrightarrow \sigma > \sigma_{0.2}\,, \tag{2}$$

where $\sigma_{1.0}$ is the 1% proof stress of the material, $n'_{0.2,1.0}$ is the strain hardening exponent, and $E_{0.2}$ is the stiffness (tangent modulus) at the 0.2% proof stress given as:

$$E_{0.2} = \frac{E_0}{1 + 0.002 \cdot n \cdot E_0 / \sigma_{0.2}} \tag{3}$$

A multilinear isotropic hardening material model (Mises plasticity) was considered for the finite element (FE) numerical analysis. A more detailed description can be found in the author's previous study [20]. However, the stress-strain behaviour was considered as ideal elastic only up to the value of 0.1 $\sigma_{0.2}$ to neglect plasticity at low strains in comparison with the value of 2/3 $\sigma_{0.2}$ considered in [20], which was too high for certain cases. The nominal stress-strain material curves were transformed into true stress and logarithmic strain dependences to match the geometric nonlinear FE analysis results:

$$\sigma_{true} = \sigma_{nom} \cdot (1 + \varepsilon_{nom}) \tag{4}$$

$$\varepsilon_{true} = ln(1 + \varepsilon_{nom})\,, \tag{5}$$

where σ_{nom} is the nominal engineering stress, ε_{nom} is the nominal engineering strain, and ε_{true} is the true total (mechanical) strain. ε_{nom} was introduced with negative values for the compressive material properties. Due to the unfeasibility of defining the negative tangent of the stress-strain relation while adopting isotropic hardening [13], the stress-strain relation was defined as ideal plastic with its tangent slope positive and close to 0 without any softening after the peak stress. Figure 2 below shows an example of the verification of the material model using the parameter values of 106×3 cross-section set – Table 3).

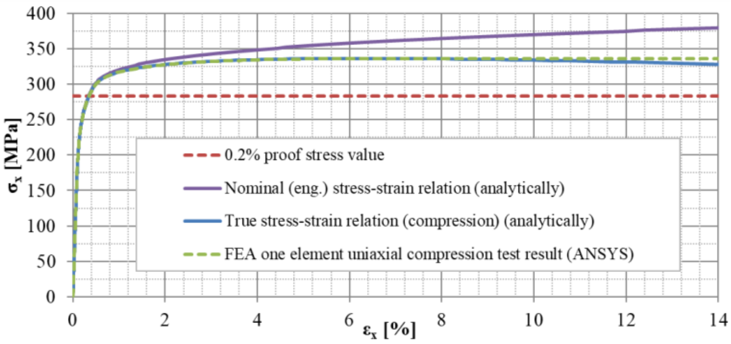

Figure 2. Verification of the material model using one element uniaxial compression test for the 106×3 set of material properties (Table 3)

Low values of membrane residual stresses have been noted in cold-formed CHS and thus can be neglected [21]. Through-thickness residual stress is included by taking into account the measured material property values [22].

IOP Conf. Series: Materials Science and Engineering 1203 (2021) 032048 doi:10.1088/1757-899X/1203/3/032048

3.5. Material property values

The set of material properties values were considered using the stub column material properties (SCP) listed in the study of Mr. Buchanan et al. [12]. These values, which are summarized below in Table 3, are based on the averaged values from all available relevant data (Table 4 in [12]).

Table 3. Summarization of considered material properties

Cross sectional set	E_0 [GPa]	$\sigma_{0.2}$ [MPa]	$\sigma_{1.0}$ [MPa]	n [-]	$n'_{0.2,1.0}$ [-]	σ_u [MPa]
106×3	196.05	283.50	323.50	8.60	3.65	615.00
104×2	202.05	359.50	407.00	4.80	2.87	726.25

3.6. Boundary conditions and loading

To simulate the pin-ended column, circumferential nodes located at the end of the CHS tube were joined in the radial direction with a single node situated on the second axis. The offset of the node is 77 mm as defined in [12] (page 301). Nodal connections were modelled using rather stiff beam elements. This boundary condition was considered at both ends of the CHS tube (see Figure 1 a and b). Loading during FE analysis was performed using a prescribed displacement of the upper node u_z (in the direction of the CHS tube axis). All translational and 2 rotational DOF of the bottom node were constrained while 2 translational and 2 rotational DOF of the upper node were constrained.

4. Results

The results of performed FE analyses for both modelling approaches, #A (shell model) and #B (solid model), which include the ultimate axial loads $N_{u,}$ ultimate mid-height lateral deflections $\omega_{u,}$ and experimental results ($N_{u,exp}$ and $\omega_{u,exp}$) [12] are tabulated in Tables 4 – 5. Validation of the FE models was performed by comparing the averaged (mean) values of the normalized ultimate loads $N_{u,\#}/N_{u,exp}$ and the averaged normalized deflections $\omega_{u,\#}/\omega_{u,exp}$ (Table 6), along with the standard deviations and the coefficient of variation of the whole set. Results of the "opposite" specimen, i.e., specimen with negative values of $\omega_{u,exp}$, were excluded (Table 4: 106×3-550-P, and Table 5: 104×2-550-P and 104×2-750-P) for the normalized deflections $\omega_{u,\#}/\omega_{u,exp}$ marked with an asterisk "*" (Table 6). The negative values of $\omega_{u,exp}$ arise because the specimens change the initial direction of the mid-height lateral deflection caused by the applied eccentricity before the peak force $N_{u,exp}$ is reached as described in [12].

The global slenderness $\bar{\lambda}$ is computed in dependence on the class of the cross-section, which is defined in EN 1993-1-4 [23]. Equation 6 is considered for classes (cl.) 1 - 3, and Equation 7 is considered for class 4 cross-sections:

$$\bar{\lambda} = \sqrt{\frac{A \cdot \sigma_{0.2} \cdot L^2}{\pi^2 \cdot E \cdot I}} \tag{6}$$

$$\bar{\lambda} = \sqrt{\frac{A_{eff} \cdot \sigma_{0.2} \cdot L^2}{\pi^2 \cdot E \cdot I}}\ , \tag{7}$$

where A is the cross-section area, $\sigma_{0.2}$ is the 0.2 % proof stress, E is Young's modulus, I is the second moment of area, L is the effective length and, A_{eff} is the effective cross-section area determined according to the formula listed in BS 5950-1 [24]:

$$A_{eff} = A \cdot \left[\left(\frac{90}{D/t} \right) \cdot \left(\frac{235}{\sigma_{0.2}} \cdot \frac{E}{210000} \right) \right]^{0.5} \tag{8}$$

The limits of the compressive class slenderness were considered according to EN 1993-1-4 [23]. The compressive classes (cl.) are listed in Tables 4 – 5.

Figure 3 illustrates the *N-ω* (axial load – mid-height deflection) curves for two selected cases. Modelling approaches #A (shell model) and #B (solid model) are compared graphically.

Table 4. Results of the cross-section set 106×3 CHS pin-ended columns

Specimen	$\bar{\lambda}$ [-]	*cl.*	$N_{u,\#A}$ [kN]	$\omega_{u,\#A}$ [*mm*]	$N_{u,\#B}$ [kN]	$\omega_{u,\#B}$ [*mm*]	$N_{u,exp}$ [kN]	$\omega_{u,exp}$ [*mm*]
106×3-550-P	0.18	1	270.6	2.61	270.2	2.40	267.0	-9.56
106×3-750-P	0.25	1	265.0	3.33	264.6	3.53	244.8	4.02
106×3-750-PR	0.25	2	249.2	3.38	248.8	3.58	242.2	4.66
106×3-950-P	0.32	1	242.9	4.74	242.5	4.70	253.4	3.76
106×3-1150-P	0.38	1	234.1	6.13	233.6	6.22	248.8	4.10
106×3-1650-P	0.55	1	198.7	7.35	198.2	7.35	201.3	7.10
106×3-2150-P	0.71	2	176.2	7.97	175.7	8.19	185.5	10.66
106×3-2650-P	0.88	2	156.6	9.84	156.1	9.25	159.4	13.27
106×3-3080-P	1.02	2	139.0	11.70	138.5	11.05	150.8	10.57

Table 5. Results of the cross-section set 104×2 CHS pin-ended columns

Specimen	$\bar{\lambda}$ [-]	*cl.*	$N_{u,\#A}$ [kN]	$\omega_{u,\#A}$ [*mm*]	$N_{u,\#B}$ [kN]	$\omega_{u,\#B}$ [*mm*]	$N_{u,exp}$ [kN]	$\omega_{u,exp}$ [*mm*]
104×2-550-P	0.21	3	228.8	2.24	228.7	2.29	241.1	-2.21
104×2-750-P	0.28	3	218.9	2.44	218.6	2.33	232.1	-1.95
104×2-950-P	0.35	3	206.7	3.68	206.4	3.48	204.2	5.17
104×2-1150-P	0.43	3	195.9	5.06	195.6	4.68	180.8	6.24
104×2-1650-P	0.62	3	163.5	10.21	163.2	10.42	154.8	10.50
104×2-2150-P	0.79	4	132.3	14.05	132.0	14.05	126.4	15.19
104×2-2650-P	0.97	4	108.5	15.35	108.2	15.65	109.0	19.40
104×2-3080-P	1.14	4	95.4	17.84	95.2	18.32	89.7	22.81

Table 6. Statistical comparison of modelling approaches #A (shell model) and #B (solid model)

Item	#A (shell FE model)	#B (solid FE model)
Mean (average) $N_{u,\#}/N_{u,exp}$ [-]	1.001	0.999
Standard deviation $N_{u,\#}/N_{u,exp}$ [-]	0.051	0.051
Coefficient of variation (COV) $N_{u,\#}/N_{u,exp}$ [%]	5.1	5.1
Mean (average) $\omega_{u,\#}/\omega_{u,exp}$ [-]	0.611	0.613
Standard deviation $\omega_{u,\#}/\omega_{u,exp}$ [-]	0.726	0.719
Coefficient of variation (COV) $\omega_{u,\#}/\omega_{u,exp}$ [%]	118.8	117.3
Mean (average)* $\omega_{u,\#}/\omega_{u,exp}$ [-]	0.924	0.922
Standard deviation* $\omega_{u,\#}/\omega_{u,exp}$ [-]	0.223	0.225
Coefficient of variation (COV)* $\omega_{u,\#}/\omega_{u,exp}$ [%]	24.1	24.4

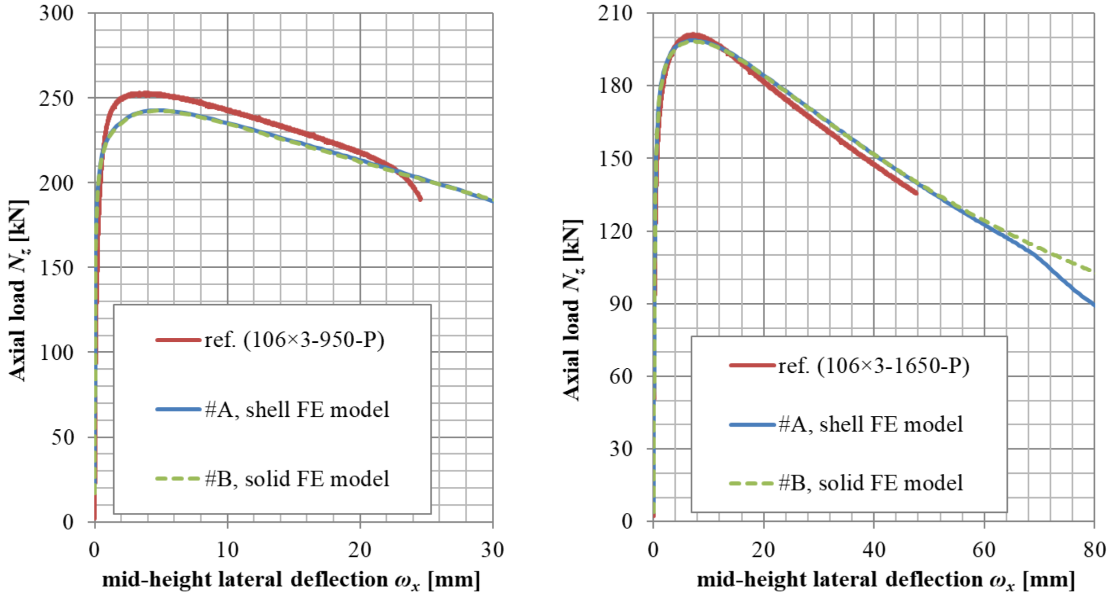

(a) (b)

Figure 3. Experimental and FE axial loads (N_z) vs. mid-height lateral deflection (ω_x) curves: (a) specimen 106×3-950-P; (b) specimen 106×3-1650-P

Figure 4 below shows the contour plots of the equivalent plastic strains for the case 106×3-1650-P. The values of deformation load u_z and corresponding axial load N_z are specified for both modelling approaches #A and #B at two stages of the analysis: at the ultimate load $N_z = N_{u,\#}$ (Figure 4, a, c), and the last analysed sub-step of the nonlinear analysis (Figure 4, b, d).

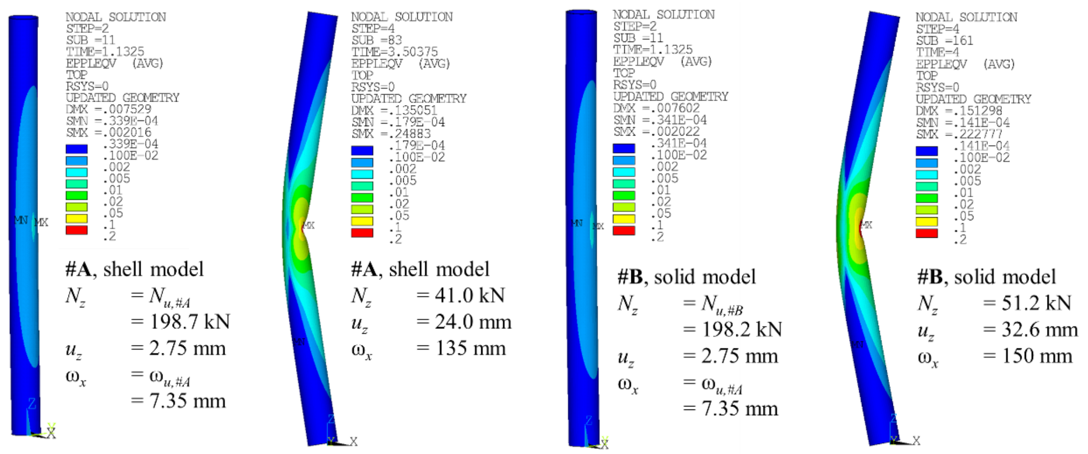

(a) (b) (c) (d)

Figure 4. Equivalent plastic strains for specimen 106×3-1650-P: (a) #A, at the ultimate load; (b) #A, last analysed sub-step; (c) #B, at the ultimate load; (d) #B, at the last analysed sub-step

5. Discussion

For longer specimens, global buckling was the most common failure mode, see Figure 4. In shorter specimens, a local buckle is developed near the mid-height of the compressed side of the tubular cross-section after the peak load has been reached. The buckling modes are comparable to those presented in the study by Buchanan et al. [12].

The comparison of the two modelling approaches, #A (shell FE model) and #B (solid FE model) is performed in the matter of the globally monitored results. The average values of the normalized ultimate loads $N_{u,\#}/N_{u,exp}$ and deflection $\omega_{u,\#}/\omega_{u,exp}$ are tabulated in Table 6 (average, standard deviation, and CoV), and are illustrated graphically in Figure 5 (average and standard deviation bars). Both of the considered modelling approaches yield essentially the same mean (average) values and coefficients of variation (CoV). The difference between the load-deflection curves depicted in Figure 3 for two chosen cases is negligible. Although the ultimate limit state is the main research interest, the behaviour of the compressed column upon reaching its load-carrying capacity is also an interesting output of the study. In several of the modelled cases, the behaviour in the post-peak softening region, where large strains were involved, varied slightly (e.g., Figure 3 b). For example, the last converged sub-step for the case shown in Figure 4 for specimen 106×3-1650-P was at the value of the axial translation u_z = 24 mm for modelling approach #A (Figure 4 b). Different values of the axial load N_z and mid-height lateral deflection ω_x (Figure 3 b) were obtained for modelling approach #B (Figure 4 d) where the analysis continued until the final value of the defined axial translation u_z = 32.6 mm.

For both modelling approaches, the mean (average) values of the ultimate axial load $N_{u,\#}/N_{u,exp}$ are quite close to the value of 1.0, and the coefficient of variation is approximately 5%. Similar results were obtained in the study performed by Mr. Buchanan et al [12] thus validating the presented finite element models.

Conversely, the mean (average) values of the ultimate lateral deflection $\omega_{u,\#}/\omega_{u,exp}$ are quite far from the value of 1.0 and the coefficient of variation is over 100% for both approaches.

The main reason for this is the opposite direction of the mid-height lateral deflection caused by the introduced eccentricity for three of the shortest specimens. Global structural response was considered in the presented finite element models. In numerical analysis, where the specimen material properties are considered the same along the whole structure, it is impossible to obtain a lateral deflection direction that is different from the direction induced by the initial global imperfection, unless some local imperfections of the material itself would be modelled. This would require modelling additional imperfections that are random and can be modelled using random fields rather than deterministically. This problem was observed only in cases of the shortest specimens with small global initial geometric imperfections, and local material imperfections might have a greater effect on the final lateral deflection direction. For longer specimens, the lateral deflection direction was identical to the direction of the initial global imperfection.

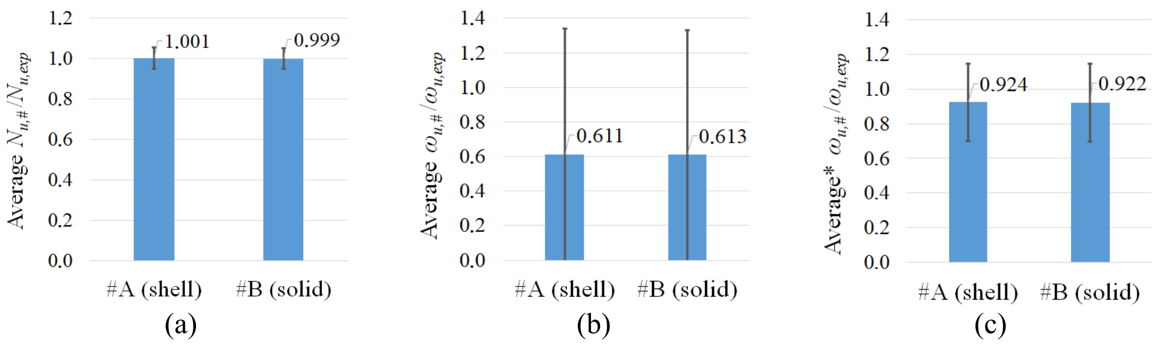

Figure 5. Average values with standard deviation bars for (a) normalized ultimate axial load, (b) normalized ultimate lateral deflection, and (c) normalized ultimate lateral deflection with the exclusion of certain specimens (3 out of 17)

Upon excluding the values of these “opposite” cases from the statistical evaluation we obtained average values of the normalized mid-height lateral deflections $\omega_{u,\#}/\omega_{u,exp}$ that was much closer to 1.0

(Figure 5 c), with better coefficients of variation (Table 6) – 24.1% (modelling approach #A) and 24.4% (modelling approach #B). The load-deflection curves are quite flat near the maximum values of the ultimate axial load. Higher values of standard deviations and coefficient of correlation can be expected in the evaluation of the results of normalized ultimate lateral deflections $\omega_{u,\#}/\omega_{u,exp}$, similarly to the study by Mr. Buchanan et al [12]. The results presented here are similar to the results in the study [12], hence these results can be considered very representative.

6. Conclusion

Stainless steel is a modern material with little information on its behaviour in load-bearing structural elements. This article fills this gap with a study that compares the load-carrying capacity and limit state deformations of several geometrically and materially nonlinear models of imperfect columns subjected to compression. The numerical models are based on SHELL 181 and SOLID 185 elements, which are some of the most efficient and well-documented finite elements of their kind available in the ANSYS program. This article describes the effects of several variant mesh sizes, models of imperfections, boundary conditions, and other model characteristics on the model outputs and describes the similarities and differences in the behaviour of the compressed column. The presented model outputs are in very good agreement with the results of experimental research, which was carried out independently at another workplace [12]. The differences between the models presented in this paper are relatively small, which confirms the rationality of the adopted approaches and opens up the possibility of use in probabilistic reliability analysis [25, 26] to explain the variance in results obtained from experimental research, which is another objective.

Acknowledgment(s)

This paper has been created with the financial support of the Czech Science Foundation by project No.: 20−00761S "Influence of material properties of stainless steels on the reliability of bridge structures". Additional financial support was provided by the BUT fund for specific university research, project number FAST-J-21-7169.

We would like to gratefully thank Mr. Craig Buchanan, Mr. Leroy Gardner, and Mrs. Esther Re-al for sharing the processed data curves of their conducted experiment. Proper validation of the numerical FE models here presented would not be possible without their generous contribution.

References

[1] P. Kotes, M. Vavrus, J. Jost, J. Prokop, “Strengthening of concrete column by using the wrapper layer of fibre reinforced concrete,” *Materials*, vol. 13(23), 5432, 2020.

[2] J. Kralik, J. Kralik, “Dynamic analysis of soil-structure interaction effects on NPP building using simplified and solid FE model of layered subsoil,” *Journal of Measurement in Engineering*, vol. 7(1), pp. 12–19, 2019.

[3] J. Chalmovsky, J. Stefanak, L. Mica, Z. Kala, S. Skuodis, A. Norkus, D. Zilioniene, “Statistical-numerical analysis for pullout tests of ground anchors,” *The Baltic Journal of Road and Bridge Engineering*, vol. 12(3), pp. 145–153, 2017.

[4] V. Rykov, D. Kozyrev, “On the reliability function of a double redundant system with general repair time distribution,” *Applied Stochastic Models in Business and Industry*, vol. 35(2), 191–197, 2019.

[5] Z. Kala, “Sensitivity analysis of carrying capacity of steel plane frames to imperfections,” *AIP Conference Proceedings*, vol. 1048, pp. 298–301, 2008.

[6] Z. Kala, J. Valeš, J. Jönsson, “Random fields of initial out of straightness leading to column buckling,” *Journal of Civil Engineering and Management*, vol. 23(7), pp. 902–913, 2017.

[7] J. Kala, Z. Kala, “Large-deflection-theory analysis of the effect of web initial curvature on the ultimate strength of steel plate girder,” *AIP Conference Proceedings*, vol. 1389, pp. 1861–1864, 2011.

[8] J. Jönsson, M. Müller, C. Gamst, J. Valeš, Z. Kala, “Investigation of European flexural and

lateral torsional buckling interaction," *Journal of Constructional Steel Research*, vol. 156, pp. 105–121, 2019.
[9] Z. Kala, J. Valeš, "Sensitivity Assessment and Lateral-torsional Buckling Design of I-beams using Solid Finite Elements," *Journal of Constructional Steel Research*, vol. 139, pp. 110–122, 2017.
[10] Z. Kala, J. Valeš, "Imperfection sensitivity analysis of steel columns at ultimate limit state," *Archives of Civil and Mechanical Engineering*, vol. 18(4), pp. 1207–1218, 2018.
[11] D. Jindra, Z. Kala, J. Kala, "Validation of stainless-steel CHS columns finite element models," *Materials*, vol. 14(7), 1785, 2021.
[12] C. Buchanan, E. Real, L. Gardner, "Testing, simulation and design of cold-formed stainless steel CHS columns," *Thin-Walled Structures*, vol. 130, pp. 297–312, 2018, ISSN: 0263-8231. doi:10.1016/j.tws.2018.05.006.
[13] Ansys, Inc. ANSYS 19.0. Canonsburg, PA 15317 U.S.A., 2018.
[14] S. Shayan, K. J. R. Rasmussen, H. Zhang, "On the modelling of initial geometric imperfections of steel frames in advanced analysis," *Journal of Constructional Steel Research*, vol. 98, pp. 167–177, 2014.
[15] W. Ramberg, W. R. Osgood, "Description of stress-strain curves by three parameters," Technical Note No. 902. *National Advisory Committee for Aeronautics*, Washington, DC., 1943.
[16] H. N. Hill, "Determination of stress-strain relations from the offset yield strength values," Technical Note No. 927. *National Advisory Committee for Aeronautics*, Washington, DC., 1994.
[17] L. Gardner, D. A. Nethercot, "Numerical modelling of cold-formed stainless steel sections," In: Mäkeläinen, et al., editors. *Proceedings of the 9th Nordic Steel Construction Conference*, Helsinki, Finland, pp. 781–789, 2001.
[18] E. Mirambell, E. Real, "On the calculation of deflections in structural stainless steel beams: an experimental and numerical investigation," J. Constr. Steel Res. 2000, 54, 109-133.…
[19] L. Gardner, D. A. Nethercot, "Experiments on stainless steel hollow sections – Part 1: Material and cross-sectional behaviour," *Journal of Constructional Steel Research,* vol. 60, pp. 1291–1318, 2004, doi:10.1016/j.jcsr.2003.11.006.
[20] D. Jindra, Z. Kala, S. Seitl, J. Kala, "Material model parameter identification of stainless steel (AISI 304L)," *26th International Conference Engineering Mechanics 2020*, pp. 246–249, 2020.
[21] R. B. Cruise, L. Gardner, "Residual stress analysis of structural stainless steel sections," *Journal of Constructional Steel Research*, vol. 64(3), pp. 352–366, 2008, doi:10.1016/j.jcsr.2007.08.001.
[22] M. Jandera, L. Gardner, J. Machacek, "Residual stresses in cold-rolled stainless steel hollow sections," *Journal of Constructional Steel Research*, vol. 64(11), pp. 1255–1263, 2008, doi:10.1016/j.jcsr.2008.07.022.
[23] European Committee for Standardization. EN 1993-1-4:2006+A1:2015 Eurocode 3 - design of Steel Structures - Part 1-4: General rules - Supplementary rules for Stainless Steels. Brussels, Belgium: 2015.
[24] British Standards Institution, BS 5950-1:2000 structural use of Steelwork in Building - part 1: Code of Practice for Design - Rolled and Welded Sections, 2000.
[25] Z. Kala, "Reliability of steel members designed in accordance with the code design concepts," *AIP Conference Proceedings*, vol. 1281, pp. 579–582, 2010.
[26] M. Krejsa, Z. Kala, S. Seitl, "Inspection based probabilistic modeling of fatigue crack progression," *Procedia Engineering*, vol. 142, pp. 146–153, 2016.